Flow Pattern and Mixing Characteristics of Highly Viscous Fluid in a Dynamic Mixer

Junhao Wang [a], Zhipeng Li [a *], Zhengming Gao [a *], J.J. Derksen [b]

[a] State Key Laboratory of Chemical Resource Engineering, School of Chemical Engineering, Beijing University of Chemical Technology, Beijing 100029, China

[b] School of Engineering, University of Aberdeen, Aberdeen AB24 3UE, UK

* E-mail address: lizp@mail.buct.edu.cn (Zhipeng Li), gaozm@mail.buct.edu.cn (Zhengming Gao).

Abstract

Computational fluid dynamics (CFD) was used to assess the flow pattern and mixing characteristics of highly viscous fluids in a dynamic mixer. The simulated concentration distribution was validated by the data measured by planar laser induced fluorescence (PLIF). The refractive indices of the two fluids and the transparent solid material comprising the mixer are matched to minimize bending of sent and received light. Simulated concentration fields agree well with measured concentration fields. The flow pattern and mixing performance were quantitatively evaluated by using the mixing index λ and the coefficient of variation (COV), respectively. After the mixing performance reaches time-independence, a reduction of COV at the outlet is associated with a slight increase of the volume averaged $|\lambda|$. The results suggest that elongational flow is more effective than shear flow in obtaining a more uniform concentration distribution in highly viscous fluids.

Keywords: Highly viscous fluid, Planar laser-induced fluorescence, Refractive index matching, Species transport, Dynamic mixer

Nomenclature

A	Area of the section, [m^2]
C	Concentration (mass fraction), [-]
$\boldsymbol{D}$	Strain rate tensor, [1/s]
D_m	Diffusion coefficient, [m^2/s]
D_{Rotor}	Diameter of the rotor, [m]
D_{Stator}	Diameter of the stator, [m]
d	Diameter of the cavities, [m]
F	Fluorescence intensity, [cd]
g	Gravitational acceleration vector, [m/s^2]
I	Excitation intensity, [cd]
N	Rotating speed, [rev/min]
n	Refractive index, [-]

p	Pressure, [Pa]
Q	Volumetric flow rate, [mL/min]
t	Time, [s]
uvw	Velocity magnitude in x, y, and z direction, [m/s]
$\boldsymbol{V}$	Vector of velocity, [m/s]
V_{tip}	Tip speed of the rotor, [m/s]
xyz	Cartesian coordinates, [m]

Greek letters

β	Angle between the rotor and stator, [°]
Δt	Time step in simulation, [s]
δ	Scalar diffusion distance, [m]
λ	Mixing index, [-]
μ	Viscosity of fluids, [Pa·s]
ρ	Density of fluids, [kg/m^3]
σ	Standard deviation, [-]
τ	Space time, [s]
$\boldsymbol{\Omega}$	Vorticity tensor, [1/s]

1 Introduction

Polymer industrial applications often require the blending of highly viscous fluids. As for the mixing in very viscous systems, it predominantly takes place under laminar conditions. The effect of laminar mixing is the key to determine the quality of polymer composites. However, the mixing process of highly viscous fluid, whose viscosity is over 10 Pa·s, is a formidable task. On the one hand, the laminar mixing pattern lacks turbulent eddies to assist species transport; on the other hand, low diffusion coefficients of highly viscous fluids with orders of magnitude around 10^{-11} m^2/s and even lower strongly limits diffusive mixing.[1].

Attempts to overcome these challenges have led to development of mixing strategies which impose deformation on the highly viscous fluid, including shear, stretching, folding, and reorientation[2]. These have been enforced by rotor against vessel wall[3], or stator[4]. The cavity transfer mixer (CTM), a dynamic mixer variant, was devised by Gale to enhance the mixing performance of polymer[5]. The CTM includes the rotor and the stator, both with a series of hemispherical cavities, as illustrated in Fig. 1. Rotor rotation causes a continuous change in the relative location of the fluid within the cavities. Simultaneously, there is a pressure driven through-flow in the CTM. The flow field induces lateral and transverse fluid motion, involving pulling, shearing, compression, folding, and reorientation by the moving geometry and pressure load.

Effective design and optimization of CTM devices demand a thorough understanding of flow patterns

and associated mixing characteristics. In demonstrating the potential of CTM for enhanced mixing, researchers, including Wang and Manas-Zloczower[6], utilized computational fluid dynamics (CFD) simulations to analyze the three-dimensional flow field within the CTM, leading to discussions on its potential for dispersive mixing in their report. Grosso et al.[7] performed a thorough numerical study to discuss the mixing performance within the CTM. The finite element solver and a mapping method was implemented to predict the concentration field. Their study underscored the significant impact of factors such as the geometric dimensions of cavities and an optimal ratio, defined as the axial and tangential velocity of the fluid, on the mixing performance of the CTM. Huang et al.[8] simulated the mixing process of Newtonian viscous fluids, assessing how the clearance between the rotor and stator influences mixing performance. Their findings suggested that a smaller gap improves mixing but results in higher energy consumption.

The quantitative visualization of highly viscous fluid flow and mixing involves the application of laser-based flow diagnostic methods. These techniques enable the measurement of mixing performance by examining the interplay between the flow field and fluid rheology. The particle image velocimetry (PIV) technique was used by Jaffer et al.[9] to measure the flow fields inside the twin screw extruder. The PIV experimental data was used to validate the simulated flow data at different flow rate, and they were in good agreement at high flow rate. These results show the feasibility of implementing optical measurement in this highly complicated geometry. Cortada-Garcia et al.[10] obtained velocity profiles in a laboratory-scale stirred tank filled with highly viscous shear thinning fluids. PIV experiments were evaluated in their study, and interrogation error was identified as the most significant error. Alberini et al.[11] used planar laser-induced fluorescence (PLIF) to examine the mixing performance of KM static mixers with highly viscous fluids. They observed that when a high viscosity liquid is mixed with a low viscosity continuous phase, a high viscosity fluid filament is transformed into a point, a phenomenon that has not been detected conventional methods.

Optical experiments on mixing (including PLIF) in dynamic and complex geometries with strongly curved walls need further investigation. The challenge in this work is how to fulfill the refractive index matching (RIM) of both working fluids themselves and working fluids with the transparent solid material of the mixer, to allow for unobstructed optical access[12,13]. PLIF images could not only display the mixing effectiveness of highly viscous fluids in the dynamic mixer at specific condition, but also validate simulations. Through this technique, the understanding of mixing quality has moved from an empirical one, relying on a single parameter to a multidimensional one, incorporating a number of factors[11].

This paper extends our earlier research on mixing highly viscous fluids in dynamic mixers [8]. Unlike the previous paper that used PIV experiments for validation, our current study presents scalar concentration distribution data measured with PLIF, providing a direct demonstration of scalar mixing. In earlier studies conducted within the dynamic mixer, the focus was on exploring the influence of buoyancy, originating from fluids with different densities, on the mixing performance. A dimensionless number, Ar/Re, calculated as the

ratio of buoyancy ($\Delta\rho gL^3$) to viscous force ($\mu\frac{U}{L}L^2$), was introduced to describe the mixing efficiency of miscible Newtonian fluids with density differences. The conclusion was drawn that mixing processes with identical Ar/Re values are essentially similar, and the greater the Ar/Re, the poorer the mixing performance.

In this work, the first purpose is to showcase the applicability of using PLIF experiments in such structurally complex environment with strongly curved walls and relative motion between components. And then, the simulation results and numerical method will be validated by comparing the experimental result with the simulated data. Thirdly, this study explored the correlation between flow patterns and mixing performance for highly viscous fluids.

This paper follows the structure outlined below: the next section introduces the flow system and the PLIF experimental setup. Following that, we provide a concise summary of the numerical approaches employed, referencing relevant literature. The results section begins by introducing the validation of simulations using PLIF experimental data. Next, we study the flow pattern within the dynamic mixer. The mixing index λ was chosen to evaluate levels of the elongational flow and shearing flow quantitively. Then, under different operation conditions, we systematically analyzed how the mixing performance is affected by the flow pattern. We attempt to relate mixing performance and λ. The concluding section summarizes key findings and discusses avenues for future research.

2 Flow system

The dynamic mixer, whose layout is depicted in Fig. 1(a), is constructed from polymethyl methacrylate (PMMA). Agitation is achieved by the cavities on the rotor and stator. In the axial direction (z-direction), there are five rows cavities on the rotor and six rows cavities on the stator. There are six rows cavities on the circumference of the rotor and stator. There are two inlets and one outlet connected to the stator through holes with a diameter of 10 mm. The two inlets are symmetrically positioned along the x/d=0 plane and are situated on the left side of the dynamic mixer, while the outlet is located at the center on the right side of the dynamic mixer. The working fluids are fed by two external gear pumps (Cixi, China) connected with the two inlets. The flow rate is determined by a preliminary calibration. There is a volumetric flow rate of 64 and 16 mL/min at inlet 1 and 2, respectively. Initially, the dynamic mixer contained liquid 1, with Inlet 1 filled with fluid 1 and Inlet 2 filled with fluid 2. The diameter of the rotor is 84 mm, and the stator has a diameter of 85 mm. Cavities of rotor and stator have a diameter of 40 mm.

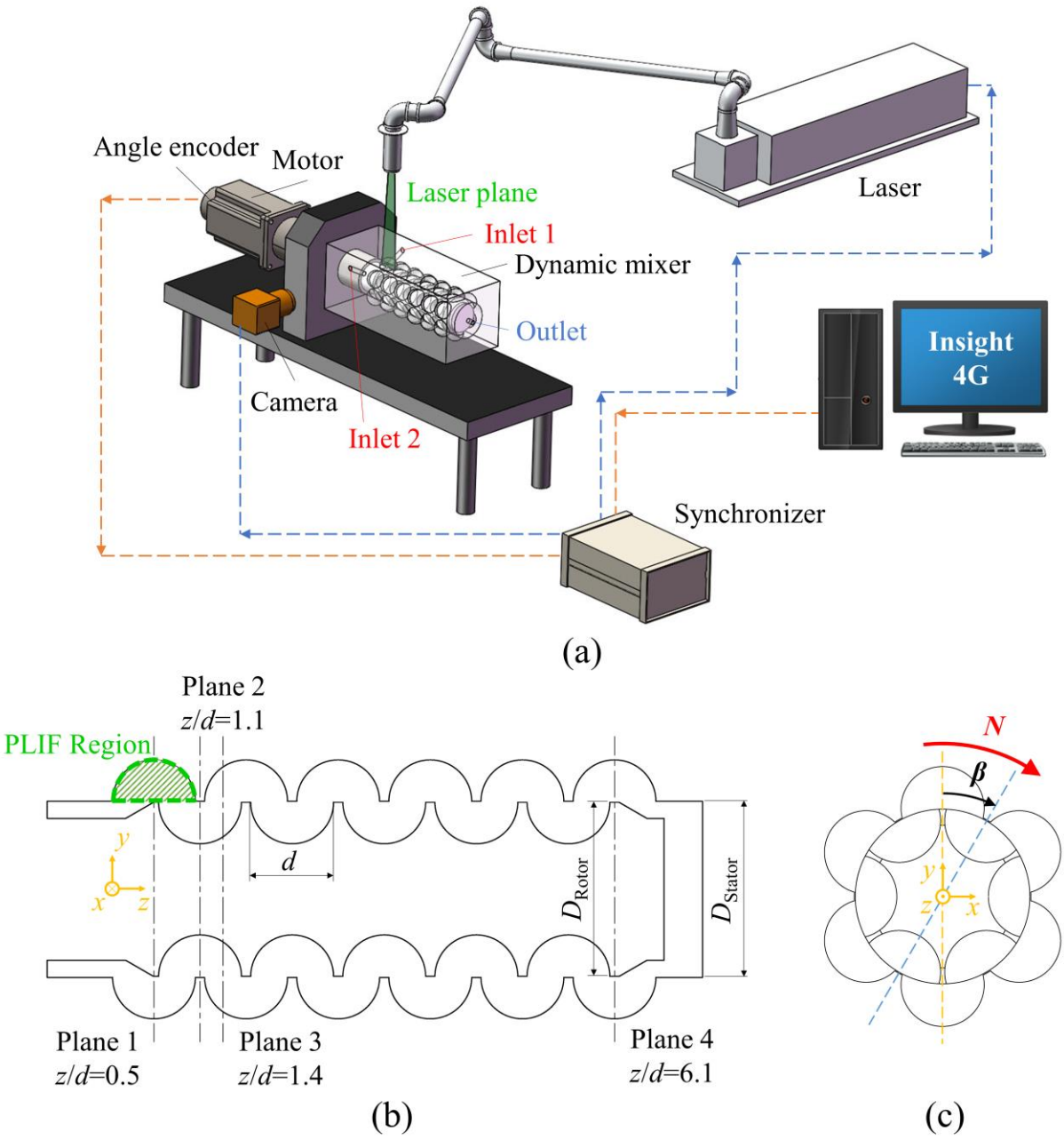

Fig. 1. (a) PLIF experimental set-up, there are six rows stator cavities and five rows rotor cavities in a three-dimensional dynamic mixer. (b) Four planes perpendicular to z-direction where we mainly show results, and the PLIF measuring region. (c) Definition of the angle β between the stator and rotor.

Computer-controlled stepping motors enforce the rotor at N=1 rev/min (CNYOHO, China). Rotor and stator positions are synchronized by an angle encoder that generates transistor-transistor logic (TTL) signals. The relative position between the rotor and stator is represented by angle β as defined in the Fig. 1(c).

The experiment temperature is exactly keeping at 21±0.5℃. The experimental study utilized a maltose aqueous solution (94.4 wt%) as both working fluid 1 and fluid 2. The solution had a density ρ of 1386 kg/m³, viscosity μ of 20 Pa·s, and refractive index n of 1.487 at 21 ℃. At constant temperature 21 °C, viscosity and refractive index were measured using a MARS40 Rheometer (Haake, Germany) and a WAY-2W Abbe refractometer (INESA, China), respectively. Optical distortion was minimized by matching the refractive index of this solution to that of PMMA (n=1.487 at 21°C).

In this experimental study, the Reynolds number is defined as $Re=\frac{\rho N D_{\text{Rotor}}{}^2}{\mu}=0.002$ indicating laminar flow. To evaluate the mixing efficiency of miscible highly viscous fluids, a critical parameter considered is the Schmidt number $Sc = \frac{\mu}{\rho D_{\text{m}}}$. Based on Zhu et al.'s[14] experimental data for maltose aqueous solution, the diffusion coefficient D_{m} is determined to be 1×10^{-11} m^2/s. In this study, the Schmidt number is calculated as 1.4×10^{9}. The Peclet number $Pe = ScRe = \frac{N D_{\text{Rotor}}{}^2}{D_{\text{m}}}$, a parameter indicating whether mass transfer is governed by diffusion or convection, surpasses 1 significantly in our study. Consequently, both the Schmidt number and Peclet number are well above 1, indicating that ~~the impact of mass diffusion on mixing efficiency is negligible~~ the mixing in this study is mainly controlled by reducing the scale of segregation through convective processes after which diffusion over very short distances (see Section 5.1) completes homogenization.

3 PLIF experimental setup

For PLIF measurements, we employed a dual-pulse laser system (200 mJ Nd: YGA, Beamtech, China) operating at a 532 nm wavelength. The optical setup included a high-resolution CMOS camera (5120×5120 pixels, TSI, America) equipped with an optical filter and synchronized using a dedicated synchronizer (TSI, America). Laser control, synchronization between the laser and camera, and data acquisition were managed through the Insight 4G software (TSI, America). To visualize the flow, the laser lightsheet was directed vertically into the cavity through a lateral wall of the dynamic mixer, as illustrated in Fig. 1(a) and (b).

For PLIF measurements, Rhodamine B served as the tracer in fluid 2, with a concentration of 50 $\mu g\cdot L^{-1}$. Rhodamine B has absorption and maximum emission wavelengths of 532 nm and 590 nm, respectively [15]. To selectively capture the excited fluorescence, a precise sharp cut-off filter was positioned in front of the camera, obstructing light with wavelengths less than 550 nm. The CMOS camera's exposure time was set at 2 ms. The shooting frequency and the time interval between adjacent laser pulses were both regulated by the angle encoder.

To obtain the absolute value of concentration, the calibration of the tracer concentration C and the fluorescence intensity F needs to be performed. Their relationship is [16]

$$F \propto \frac{I}{1+I/I_{\text{sat}}}C \tag{1}$$

where I_{sat} is the saturation intensity for the colorant. Since $I \ll I_{\text{sat}}$, Eq. 1 will be converted to

$$F \propto IC \tag{2}$$

Fig. 2 depicts the fluorescence intensity at the measurement plane as a function of Rhodamine B concentration, ranging from 0 to 50 $\mu g\cdot L^{-1}$. This representation reveals a clearly established linear correlation. Consequently, the camera-recorded fluorescence intensity provides a direct indicator of the concentration of the fluid containing Rhodamine B (fluid 2).

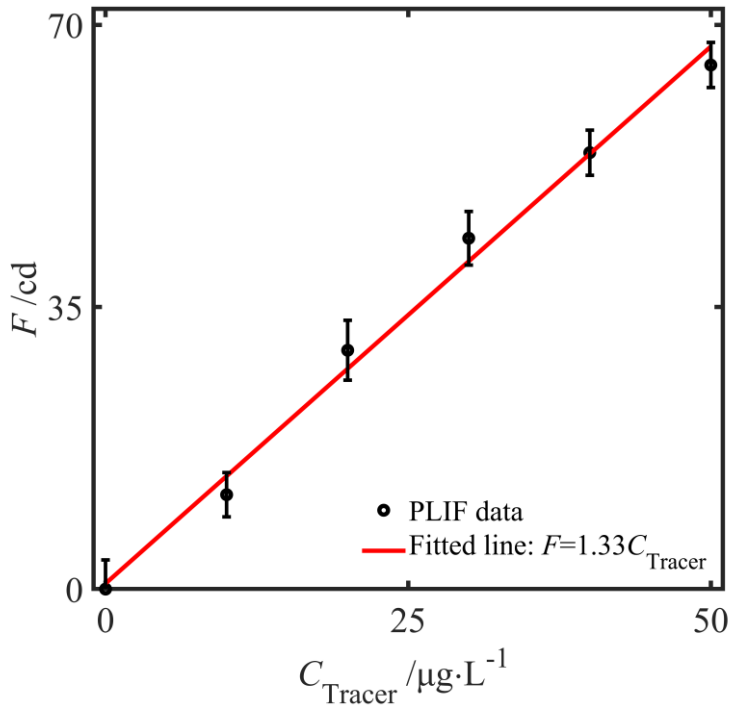

Fig. 2. The fluorescence intensity of Rhodamine B plotted against the tracer concentration in the working fluid at 21°C. The error bar, denoting one standard deviation, reveals an uncertainty of 0.059 in the 1.33 coefficient.

4 Simulation

4.1 Governing equation

The conservation of mass and momentum for Newtonian fluid were described by the continuity equation and Navier-Stokes equation:

$$\nabla \cdot \boldsymbol{V} = 0 \tag{3}$$

$$\frac{\partial \boldsymbol{V}}{\partial t} + \boldsymbol{V} \cdot \nabla \boldsymbol{V} = -\frac{\nabla p}{\rho} + \nabla \cdot \left[\frac{\mu}{\rho}(\nabla \boldsymbol{V} + \nabla \boldsymbol{V}^T)\right] + \boldsymbol{g} \tag{4}$$

where ρ is the density, $\boldsymbol{V}$ is the velocity, p is the pressure, $\boldsymbol{g}$ represents the acceleration due to gravity, and it is assigned a value of 9.81 m/s^2 in negative y direction.

The simulation of two miscible highly viscous fluids mixed in the dynamic mixer used a species transport model. The conservation equation for fluid 1 gotten by Irani and Adamson [17], is given by

$$\frac{\partial C_1}{\partial t} + \boldsymbol{V} \cdot \nabla C_1 = \nabla \cdot (D_m \nabla C_1) \tag{5}$$

where C_1 is the mass fraction of fluid 1. The mass fraction of fluid 2 is:

$$C_2 = 1 - C_1 \tag{6}$$

4.2 Numerical details

In this study, the geometrical configuration utilized by CFD simulations was the same as that employed

in the PLIF experiments. Polyhedral cells were created utilizing the commercial software Fluent Meshing, as shown in Fig. 3. In comparison to tetrahedral cells, polyhedral cells offer clear advantages in computational efficiency and precision[18]. We conducted thorough grid independence studies, the results of which will be presented in the next section.

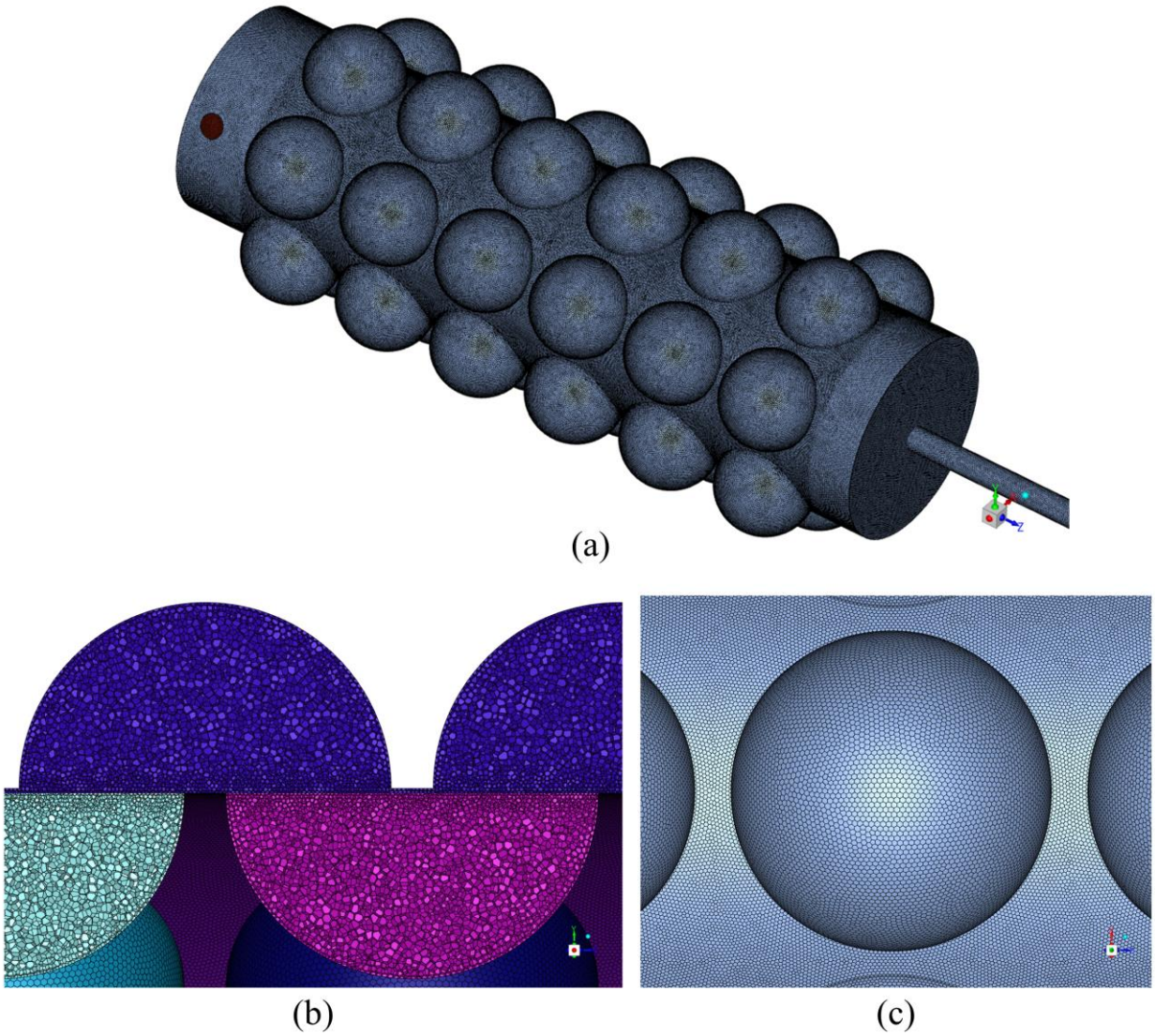

Fig. 3. The polyhedral mesh for the simulation. (a) The surface grid of the dynamic mixer; (b) the volume grid in the cavities; (c) the grid on the surface of the cavity.

As this simulation focuses on laminar incompressible flows, the Ansys Fluent software was employed with a pressure-based solver. The simulation of rotor motion employed the sliding mesh technique. The spatial discretization for species conservation equations used the third-order MUSCL scheme[19]. Coupling pressure and velocity was achieved through the SIMPLE algorithm. The second-order implicit scheme was used for time advancement. All wall boundaries were maintained under a no-slip condition. To ensure a Courant–Friedrichs–Levy number below 1 for varying angular velocities[20], the time step Δt varied from 0.1 to 0.025 s. The simulations were performed on a high-performance computer equipped with two Intel Xeon Gold 6240 CPUs and 128 GB of memory. The case with 4 million cells required approximately 12 hours for a revolution.

5 Result and discussion

5.1 Validating simulated concentration through PLIF data

The concentration fields of the PLIF experiment and CFD simulation in the plane x/d=0 at β=0° is illustrated in Fig. 4. The progression of the simulated concentration distribution concerning the dimensionless time tN, denoting the rotor's revolution, will be discussed later in Fig. 6.

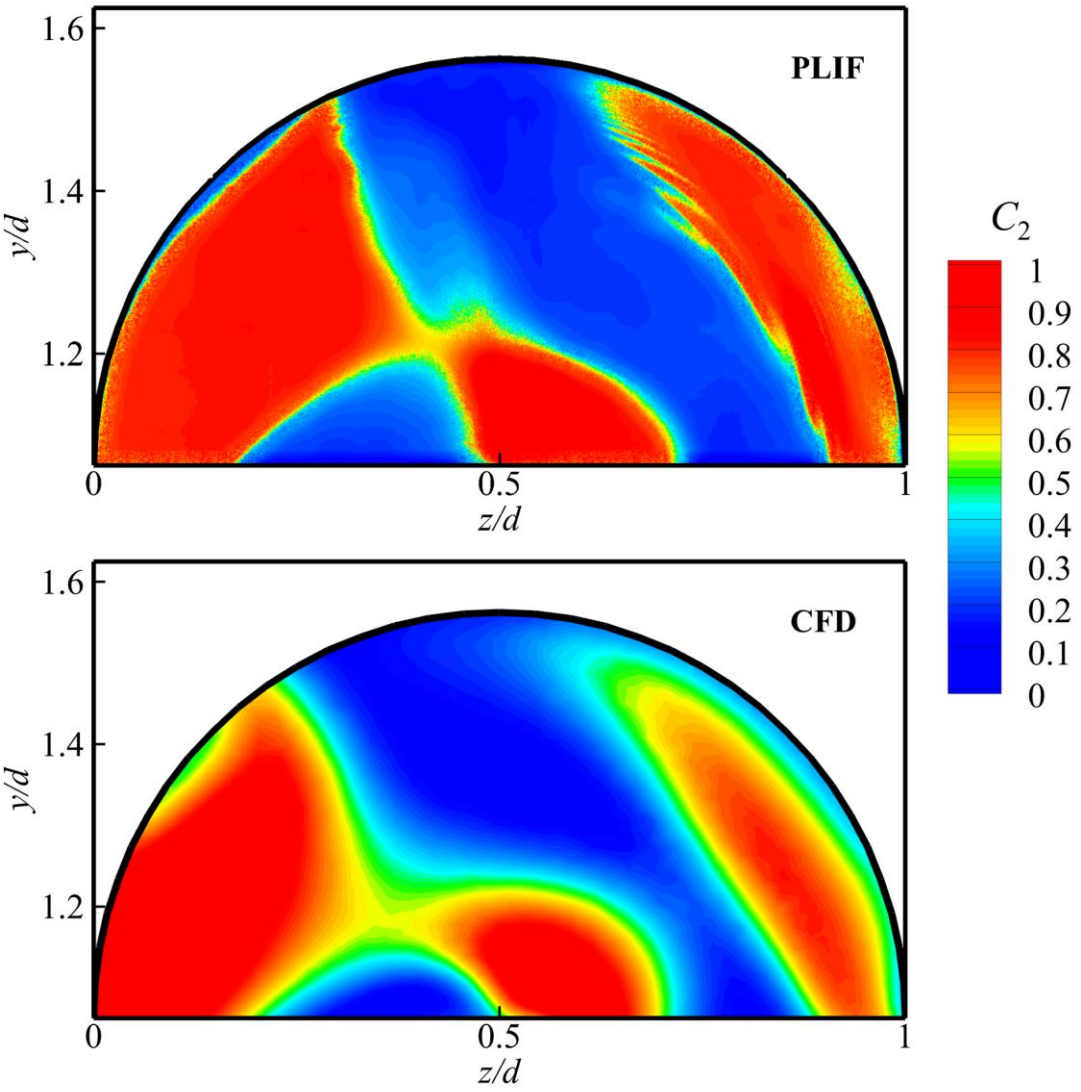

Fig. 4. Experimental (top panel) and simulated (bottom panel) concentration fields of fluid 2 in the stator cavity at β=0°, Q=80 mL/min, N=1 rev/min, and μ=20 Pa·s. The PLIF experimental results represent the mean concentration field derived from 100 frames measured at the identical angle β. On the other hand, the simulated data, based on 4 million cells, presents an instantaneous concentration field at tN=10.

To quantitatively assess the disparity between the experimental data and simulated results, concentration profiles are presented in Fig. 5 along a vertical line at z/d=0.45 and a horizontal line y/d=1.3. Minor discrepancies are observed, for example, the peak values of PLIF are higher than those of CFD at y/d=1.2 in the left panel and z/d=0.8 in the right panel. In general, the concentration results of simulation agree well with

that of experiment.

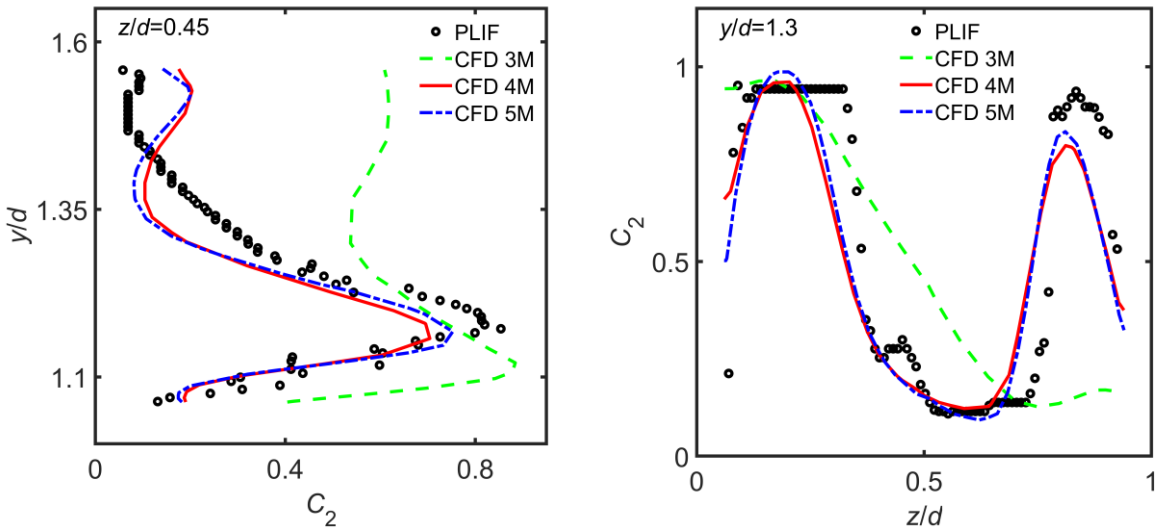

Fig. 5. Comparison of PLIF experimental and simulated concentration profiles of fluid 2 is presented for a vertical line z/d=0.45 and a horizontal line y/d=1.3 at β=0°, Q=80 mL/min, N=1 rev/min, and μ=20 Pa·s. Simulated results with 3, 4, and 5 million cells are denoted as CFD 3M, 4M, and 5M, respectively.

In addition, the simulated concentration profile with different grids can been seen in Fig. 5. As we reported in our previous work [8], the concentration field exhibits greater sensitivity to cell spacing compared to the velocity field. A smaller cell size results in a more precise simulated concentration distribution. Given Sc of 1.4×10^{9} mentioned above, the distance of scalar diffusion δ over a characteristic flow time d/V_{tip} could be calculated as $\delta/d = (\mathrm{ScRe})^{-0.5} = 2.99\times10^{-4}$. Consequently, to fully acquire concentration details, the total amount of cells within a cavity would be on the order of $\frac{4}{3}\pi(0.5\times d/\delta)^3 \approx 10^{10}$, a scale beyond current computational capabilities. As illustrated in Fig. 5, the simulated concentration profiles, utilizing 4 million cells, demonstrate a favorable alignment with the experimental results. Further increasing the number of cells did not lead to significant improvements, and further increasing cells did not lead to further development. Consequently, the subsequent simulations were performed using 4 million cells, which is a trade-off between accuracy and computational cost.

As shown in Fig. 6, concentration profiles were simulated with different time steps Δt at β=0° and tN=10. This figure shows that the profiles completely overlap along the vertical line z/d=0.45 and the horizontal line y/d=1.3. which confirms time step independence. In later simulations, the time step is 0.1 s at N=1 rev/min. To maintain constant Courant–Friedrichs–Levy number (around 0.185), the Δt varied from 0.1 to 0.025 s with rotating speed ranging from 1 to 4 rev/min.

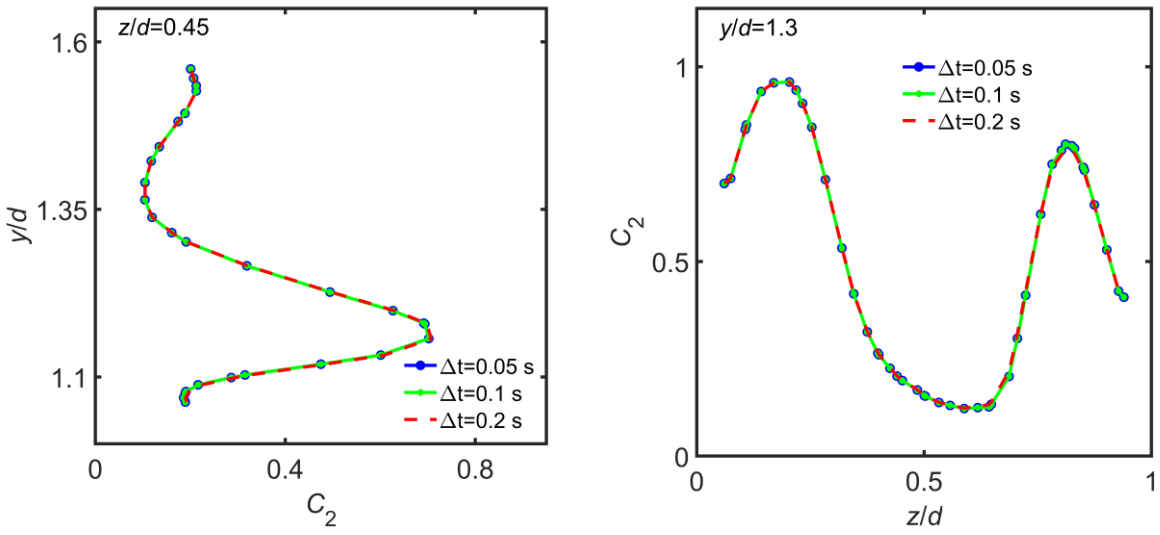

Fig. 6. Instantaneous concentration profiles of fluid 2 with different time steps Δt at β=0° and tN=10 on a vertical line z/d=0.45 and a horizontal line y/d=1.3. The operation condition is Q=80 mL/min, N=1 rev/min, and μ=20 Pa·s.

The instantaneous concentration profiles on the vertical and horizontal lines at different time are shown in the Fig. 7. The concentration profiles after 10 revolutions overlap those after 15 revolutions, that is, the concentration field becomes steady after 10 revolutions. Thus, we previously compared the experimental result with the simulated result after a steady state was reached. Notably, given that the fluid region in the dynamic mixer periodically changes with angle β, the simulation is inherently transient. In this context, "steady" implies that the flow field at the same angle β has reached full development.

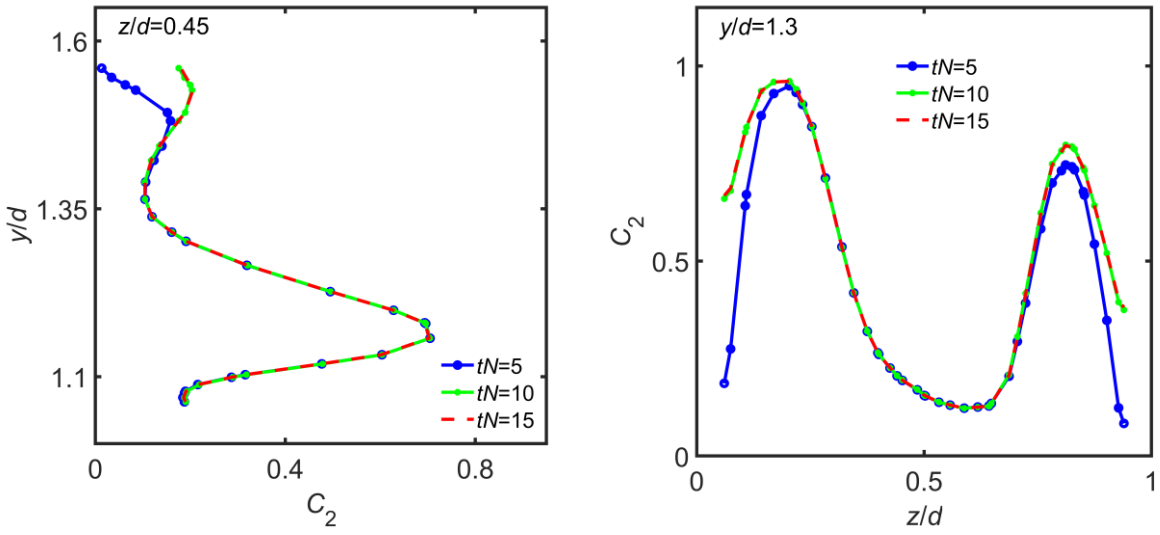

Fig. 7. Instantaneous concentration profiles of fluid 2 at β=0°on a vertical line z/d=0.45 and a horizontal line y/d=1.3 at tN=5, 10, 15, respectively. The operation condition is Q=80 mL/min, N=1 rev/min, and μ=20 Pa·s.

5.2 Flow pattern in the dynamic mixer

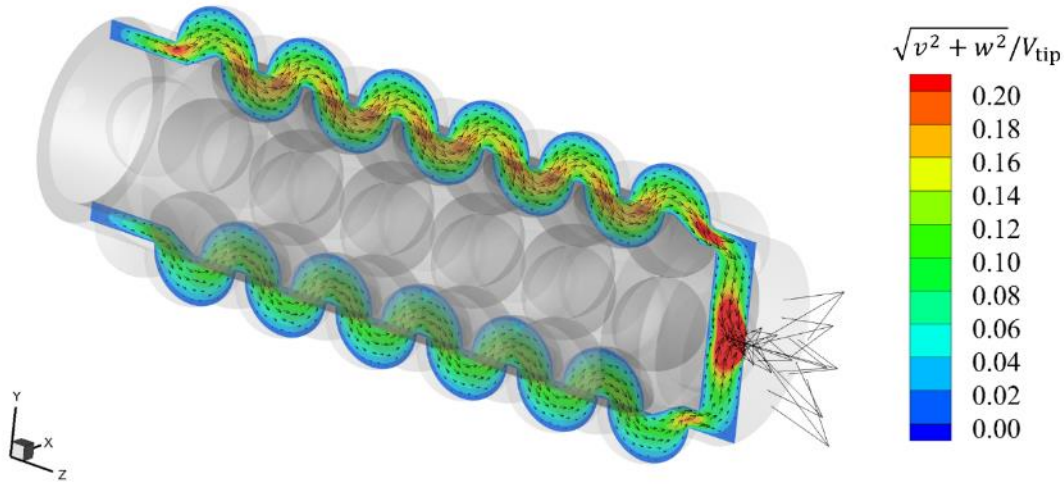

Fig. 8. Simulated steady velocity field in x/d=0 plane at β=0°, Q=80 mL/min, N=1 rev/min, and μ=20 Pa·s.

The simulated flow pattern of the dynamic mixer along the axial direction is visualized in Fig. 8. In general, the fluid moves propelled by the pressure disparity between the inlets and the outlet. During this journey from inlets to outlet, the fluid is pumped into a row of stator cavities first, and then it is squeezed into rotor cavities, subsequently to the next row of stator cavities and so on. Simultaneously, as the rotor revolves, transporting the fluid in the circumferential direction, the axial flow within the dynamic mixer exhibits periodic behavior. The flow channel between cavities of rotor and stator varies with β, which is defined in Fig. 1(c). It is noticeable that the area of overlapping region of fluid reaches the maximum at β=0°.

To clearly show the dynamic process in the axial direction, Fig. 9 illustrates a variety of local flow patterns within a period ($0° \leq \beta < 60°$). As a result of the combined motions caused by pressure driven flow and rotor rotation, the fluid undergoes a sequence of concentrations and expansions. This process involves repetitive stretching and stacking, contributing significantly to the mixing of the highly viscous fluid.

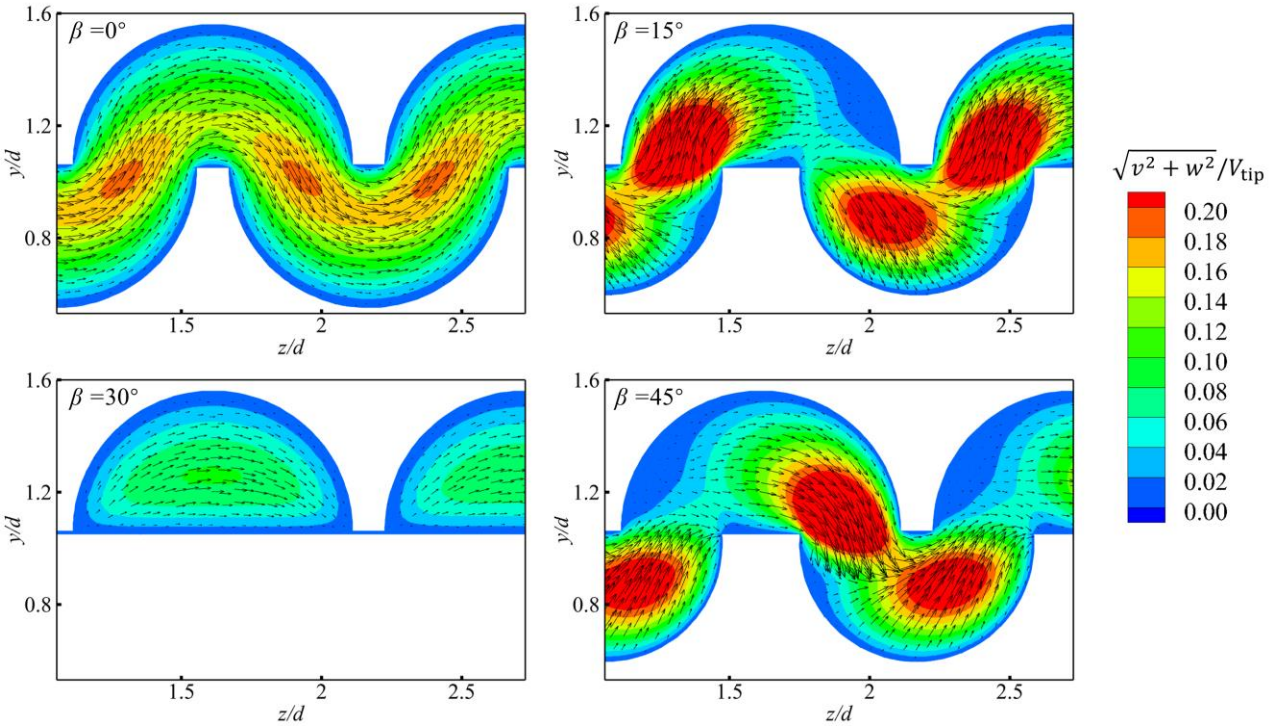

Fig. 9. Simulated local velocity field for different angle β between stator and rotor in x/d=0 plane at Q=80 mL/min, N=1 rev/min, and μ=20 Pa·s.

In the circumferential direction, the geometry, and consequently the flow, exhibit a periodicity of 60 degrees. Fig. 10 displays four representative flow patterns by depicting the dimensionless velocity distribution in the z/d = 1.4 plane over one period (a to c and f). The flow patterns within stator cavities and rotor cavities vary with the angle β, leading to a diverse array of manners in fluid transmission between cavities. To clearly depict the fluid flow between stator cavities and rotor cavities, the fluid velocity in the rotating region is presented as relative velocity based on the rotor. At $\beta = 0^{\circ}$, the cavity of stator and rotor is aligned in axial direction, and the current stator cavity pointed by blue arrow is not connected with trailing stator cavity by the rotor cavity pointed by red arrow. When $\beta = 15^{\circ}$, the fluid circulates within both the stator and rotor cavities, propelled by the shear flow generated by the combined effects of the fluid within the cavities and the cavity walls. As the rotor rotates to $\beta = 30^{\circ}$, the current rotor cavity connects the leading stator cavity and the trailing stator cavity, and fluids obviously transfer in the circumferential direction. The vortex center of fluid in cavities moves towards the middle of the stator cavity, resulting in an increase in velocity. When $\beta = 45^{\circ}$, the vortex center in the stator cavity keeps moving clockwise while in the rotor cavity, it moves in the opposite direction. Meanwhile, the connection between stator cavities and rotor cavities in the circumferential direction breaks down, resulting in a weakening of the circulation flow.

The flow pattern also varies with the axial direction, see Fig. 10 (d) to (f). Compared with the flow pattern at z/d = 1.4, that at z/d = 0.5 and z/d = 1.1 both present no overlap between cavities of rotor and stator at the circumferential cross sections. For the former, the circulation flow in the stator cavities is only caused by the rotor itself. For the latter, the velocity in the rotor cavities is high, and decreases near the stator wall because

of the boundary effect. In addition, we note here that the flow field in each cavity is markedly different from each other in the circumferential cross sections. This is due to the feeding flow rate at inlet 1 is 4 times bigger than that of inlet 2. Overall, in the circumferential cross sections, simulated flow fields present that the fluid flow experiences extension, shearing, and stacking of highly viscous fluid to promote transfer phenomenon.

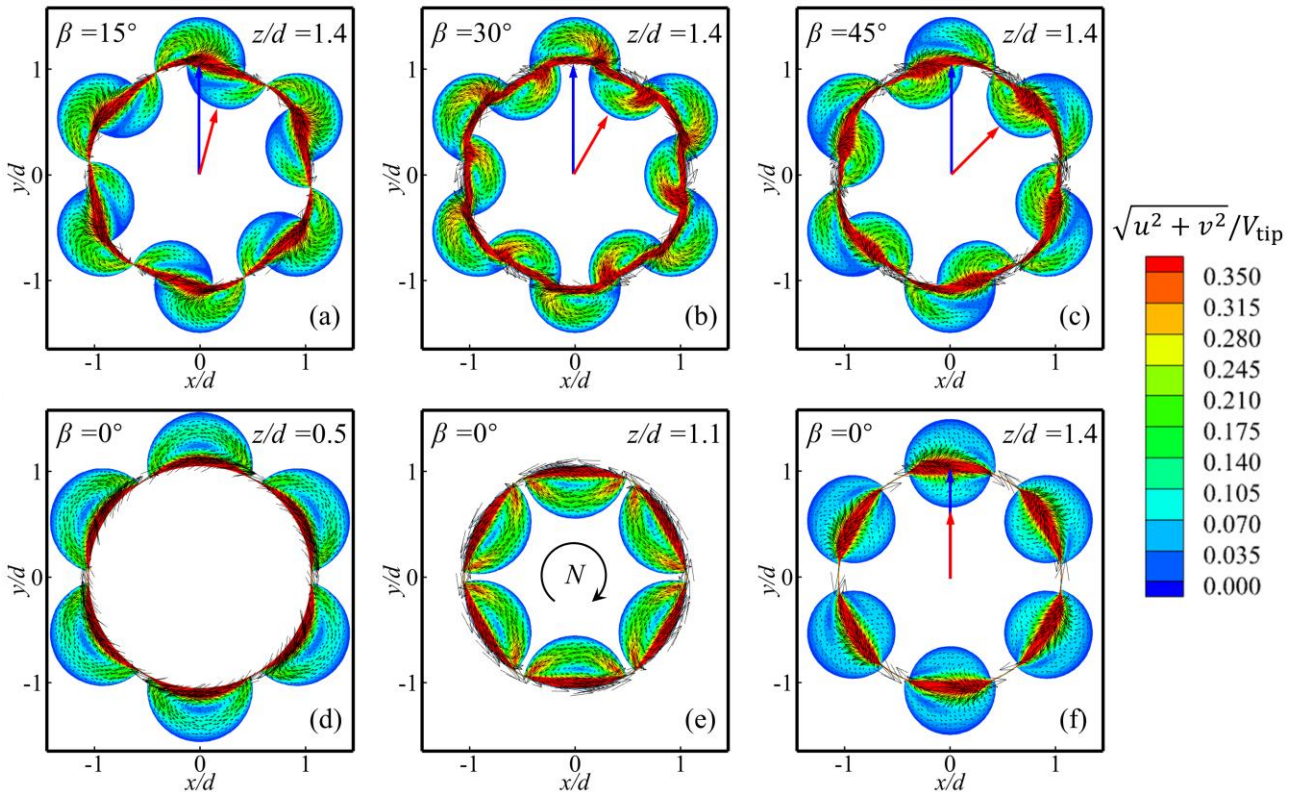

Fig. 10. Simulated velocity field in stator and rotor for different angles β and axial planes at Q=80 mL/min, N=1 rev/min, and μ=20 Pa·s. (a) z/d=1.4, β=15°; (b) z/d=1.4, β=30°; (c) z/d=1.4, β=45°; (d) z/d=0.5, β=0°; (e) z/d=1.1, β=0°; (f) z/d=1.4, β=0°. The flow in stator cavities is in a fixed reference frame and in the rotor cavities is in a reference frame rotating with the rotor. The blue arrow points towards the stator cavity, while the red arrow points towards the rotor cavity.

The mixing behavior is attained through the fluid flow generated in the mixer. Therefore, the mixing effectiveness is related to the flow pattern in the dynamic mixer. Characterizing the flow patterns is essential for obtaining insight into the performance of the dynamic mixer.

In a mixing device, the local rate of deformation is influenced by a blend of shear flow, elongational flow, and rotational flow. The velocity gradient $\nabla \boldsymbol{V}$ can be decomposed into two parts in the following identity

$$\nabla \boldsymbol{V} = \underbrace{\frac{1}{2}(\nabla \boldsymbol{V} + \nabla \boldsymbol{V}^T)}_{\boldsymbol{D}} + \underbrace{\frac{1}{2}(\nabla \boldsymbol{V} - \nabla \boldsymbol{V}^T)}_{\boldsymbol{\Omega}} \tag{7}$$

The first term on the right-hand side is the strain rate tensor $\boldsymbol{D}$, and the second term is the vorticity tensor $\boldsymbol{\Omega}$. The effectiveness of elongational flows in laminar mixing has been widely acknowledged [1]. To quantify the

level of elongational flow, the mixing index λ is defined as [21]

$$\lambda = \frac{3\sqrt{6}\,\det \boldsymbol{D}}{(\boldsymbol{D}:\boldsymbol{D})^{3/2}} \tag{8}$$

For λ=1 is a uniaxial elongational flow for fluids converging; λ=-1 is a biaxial elongational flow for fluids bifurcating; and λ=0 is a planar shear flow. Under general conditions 0<|λ|<1, the flow pattern results from a superposition of both elongational and shear flows.

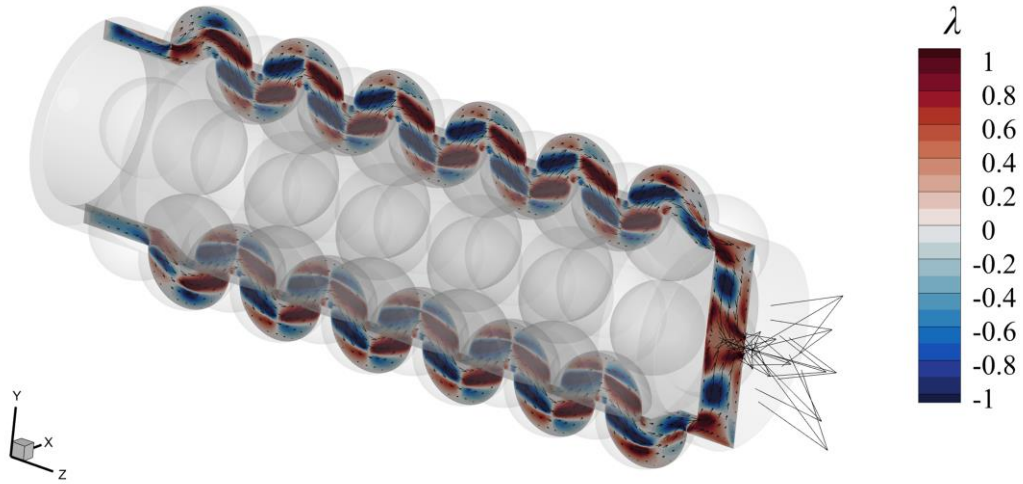

Fig. 11. Simulated distribution of the mixing index λ in x/d=0 plane at β=0°, N=1 rev/min, Q=80 mL/min and μ=20 Pa·s.

Fig. 11 presents the distribution of λ in the x/d=0 plane along the entire length of the mixer. The fluid experiences shearing flow as a consequence of the relative motion of the rotor and stator walls. The fluid experiences repetitive convergence and divergence between the rotor cavities and stator cavities, leading to a highly elongational flow. Fluid elements move back and forth within the elongational flow region, repeatedly bifurcating and converging, providing numerous opportunities for stretching and stacking. When the fluid flows in the cavity, it is divergent (λ=-1) and stacked with adjacent fluids; when the fluid flows out the cavity, it is convergent (λ=1) and stretched by the narrow configuration. The distribution of λ is periodic in the axial direction, consistent with the periodic flow pattern. However, the contour of λ is not symmetric along the center line of the mixer due to the asymmetric feed flow.

Fig. 12 shows the local distribution of λ with different β in the x/d=0 plane. Depending on β, the flow pattern along the axial direction varies, leading to diverse λ distributions for the fluid. It could be observed clearly that the region of λ<0 and λ>0 is periodic and alternating, which means fluids go through convergence and divergence repeatedly in the elongational flow. As variations in the cavity configuration with β, the region of elongational flow (strongly positive and negative λ) always coincides with the region of fluid flowing at high velocity. This suggests that elongational flow is the dominant flow pattern along the axial direction.

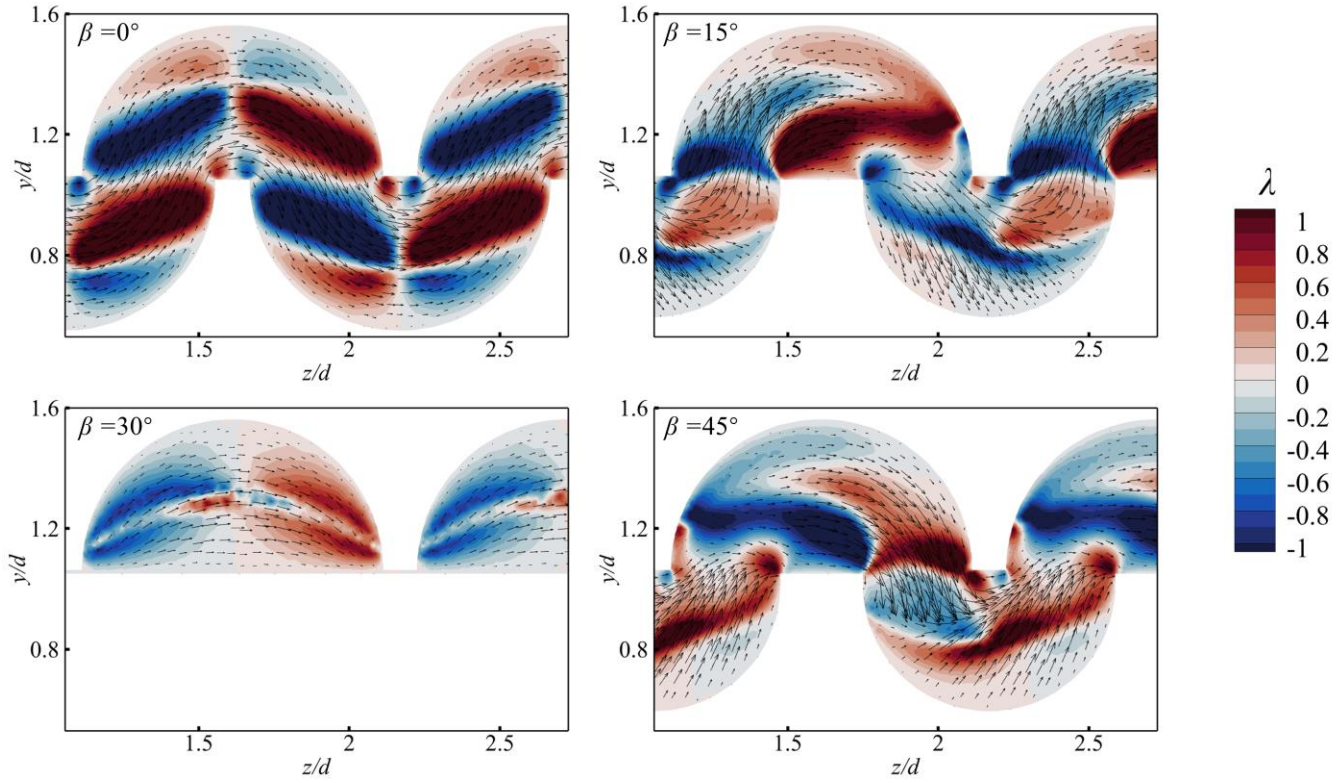

Fig. 12. Simulated local distribution of the mixing index rate λ for different angle β between stator and rotor in x/d=0 plane at N=1 rev/min, Q=80 mL/min, and μ=20 Pa·s.

Fig. 13 shows the distribution of λ in the circumferential cross sections. Similar to the flow characteristic, the distribution of λ varies in space and time. The distribution of λ varies with the location and shape of the vortex in the recirculating fluid as the rotor rotates. The fluid near the walls of the stator and rotor cavities experiences strong shear indicated by λ values close to zero, while the fluid on the recirculating path undergoes stretching and stacking. It is worth noting that the region of high velocity magnitude in Fig. 10 largely overlaps with the region of the elongational flow. In other words, the main fluid flow in the dynamic mixer is predominantly an elongational flow rather than a shearing flow.

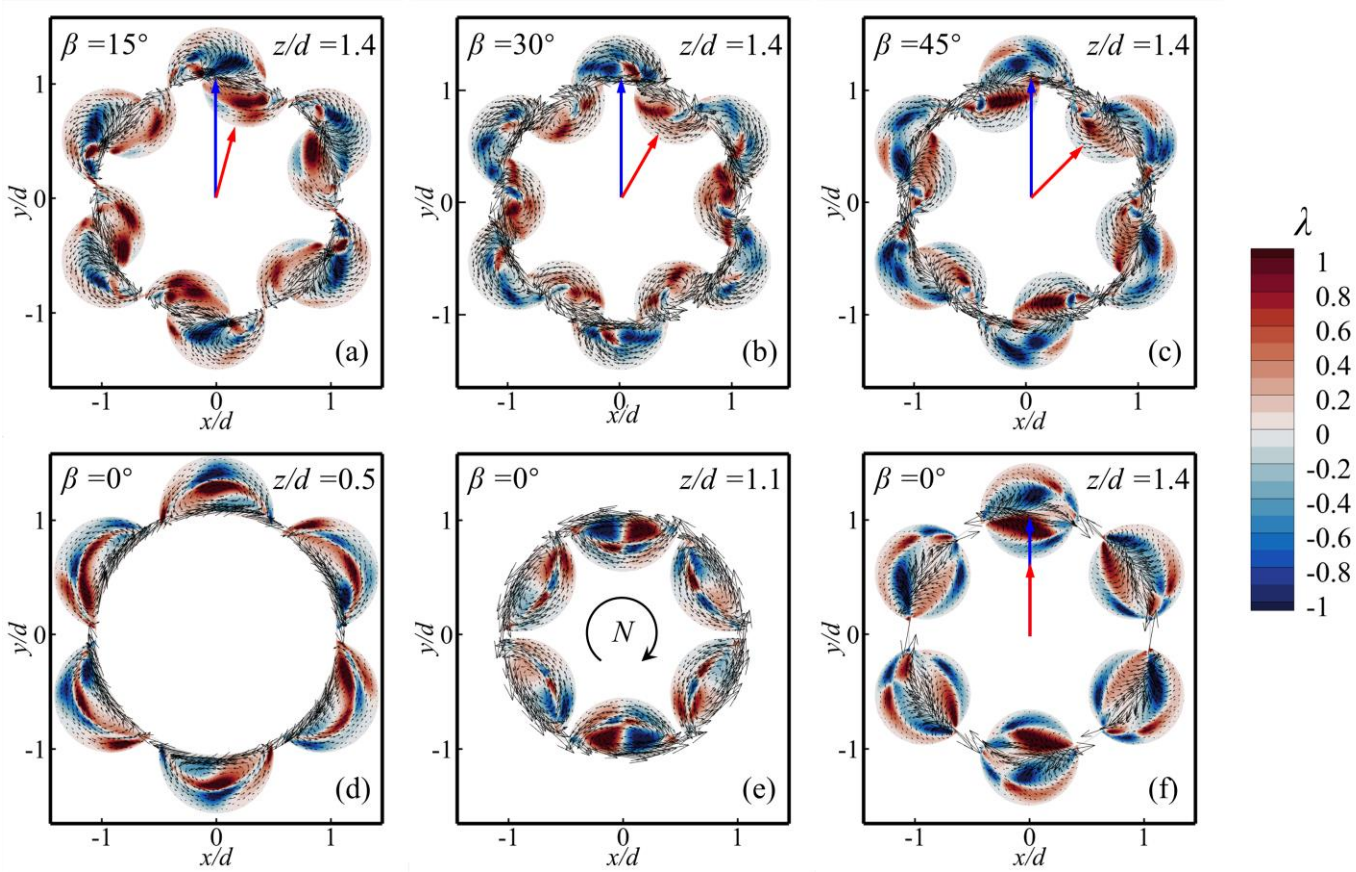

Fig. 13. Simulated distribution of the mixing index λ for different angles β and axial planes at N=1 rev/min, Q=80 mL/min, and μ=20 Pa·s. (a) z/d=1.4, β=15°; (b) z/d=1.4, β=30°; (c) z/d=1.4, β=45°; (d) z/d=0.5, β=0°; (e) z/d=1.1, β=0°; (f) z/d=1.4, β=0°.

5.3 Mixing characteristic in the dynamic mixer

To explore the influence of operation condition on the mixing process of highly viscous fluids within the dynamic mixer, a series of simulation cases were conducted, considering different feeding flow rates, rotating speeds, and fluid viscosities. The simulation settings in this section is listed in Table 1.

Table 1. Numerical Simulation Settings

Case	N (rev/min)	V_{tip} (m/s)	Q (ml/min)	ρ (kg/m3)	μ (Pa·s）	M_1(wt%)
1	1	1.85×10^{-3}	320	1386	20	80
2	1	1.85×10^{-3}	480	1386	20	80
3	1	1.85×10^{-3}	640	1386	20	80
4	2	8.80×10^{-3}	640	1386	20	80
5	4	1.76×10^{-2}	640	1386	20	80
6	1	1.85×10^{-3}	640	1386	60	80
7	1	1.85×10^{-3}	640	1386	100	80

The quantitative description of mixing efficiency is characterized by the coefficient of variation (COV) within sections of the dynamic mixer[22]:

$$\mathrm{COV} = \frac{\sigma}{\bar{C}} \tag{9}$$

$$\sigma = \sqrt{\frac{\iint_A (\bar{C} - C_i)^2 dA}{A}} \tag{10}$$

$$\bar{C} = \frac{\iint_A C_i dA}{A} \tag{11}$$

Where σ is the standard deviation, $\bar{C}$ represents the average concentration over a chosen section, and A is the area of the section (m^2). The smaller the COV, the more uniform concentration field.

To investigate the relationship between the flow pattern and the mixing characteristic, the absolute value of the mixing index $|\lambda|$ with different operation conditions were also calculated. The value of $|\lambda|$ is zero for a planar shear, unity for a pure elongational flow, and $0 < |\lambda| < 1$ for situations in between these two extremes. The volume averaged $|\lambda|$ can be calculated by the following equation:

$$\overline{|\lambda|} = \frac{\iiint_V |\lambda_i| dV}{V} \tag{12}$$

where $\overline{|\lambda|}$ is the volume average $|\lambda|$ in the dynamic mixer, V is the fluid volume of dynamic mixer.

The time is normalized by the mean residence time τ of the dynamic mixer, yielding the dimensionless time:

$$\frac{t}{\tau} = \frac{t}{V/Q} \tag{13}$$

where Q is the sum of the flow rate in the two inlets.

5.3.1 Effect of feeding flow rate on mixing performance

As shown in the left panel of Fig. 14, the mixing performance of the highly viscous fluids improves with the decreasing feeding flow rate in the dynamic mixer. Additionally, the COV curve for higher feeding flow rates stabilizes more rapidly.

To investigate the influence of feeding flow rate on the mixing process, both the volume-averaged $|\lambda|$ and the instantaneous COV after the mixing has become steady are depicted in the right panel of Fig. 14. With an increase in the flow rate, there is a decrease in the volume-averaged $|\lambda|$, and simultaneously, the COV increases. This suggests that, as the flow rate increases, a larger portion of the dynamic mixer is dominated by shearing flow, which exhibits lower mixing efficiency compared to elongational flow.

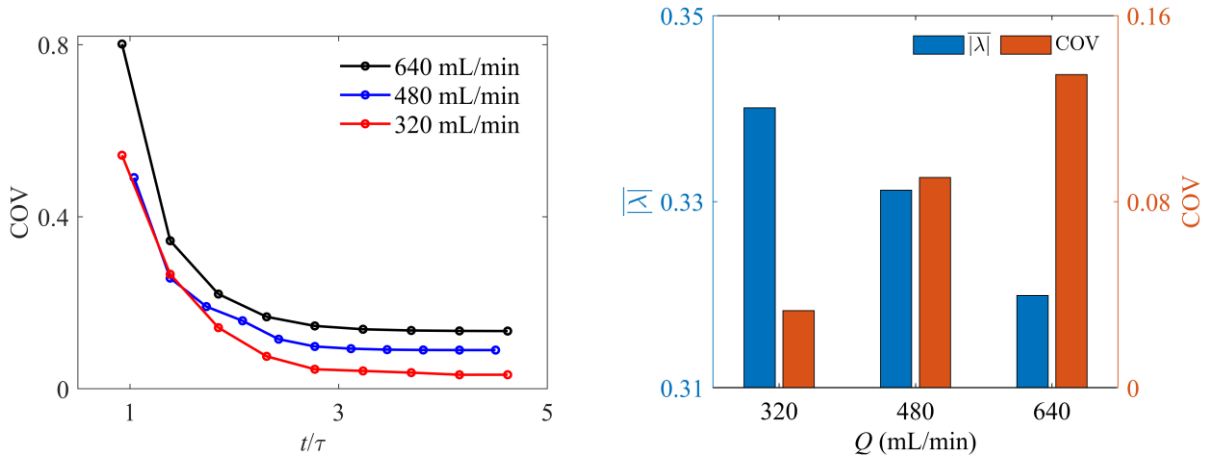

Fig. 14. Left panel: instantaneous COV of fluid 2 in the outlet plane at three feeding flow rate Q. Right panel: the volume averaged $|\lambda|$ and COV of fluid 2 in the outlet plane at three feeding flow rates with t/τ=4.5. The operation condition for the two panels is N=1 rev/min, μ=20 Pa·s.

5.3.2 Effect of rotor rotating speed on mixing performance

The influence of rotor rotating speed on the mixing process in the dynamic mixer is shown in the left panel of Fig. 15. At the end of the curves, it is evident that the COV value decreases with the increase in rotor rotating speed, indicating a increase in mixing performance.

In the right panel of Fig. 15, the volume averaged $|\lambda|$ and the COV value at outlet has become stable. With a higher rotating speed, the highly viscous fluid experiences a stronger elongational flow, resulting in a lower COV value at the same time. Undoubtedly, higher rotating speeds result in stronger shear near the rotor-stator interface. If we assume the elongational flow remains constant, according the definition of $|\lambda|$, it should decrease with the increasing rotating speeds. However, in Fig. 15, the $|\lambda|$ increases with the rotating speed, suggesting that the increase in the degree of elongational flow is larger than that of shear flow. In other words, the flow pattern associated with higher rotating speed enhances the mixing process in the dynamic mixer.

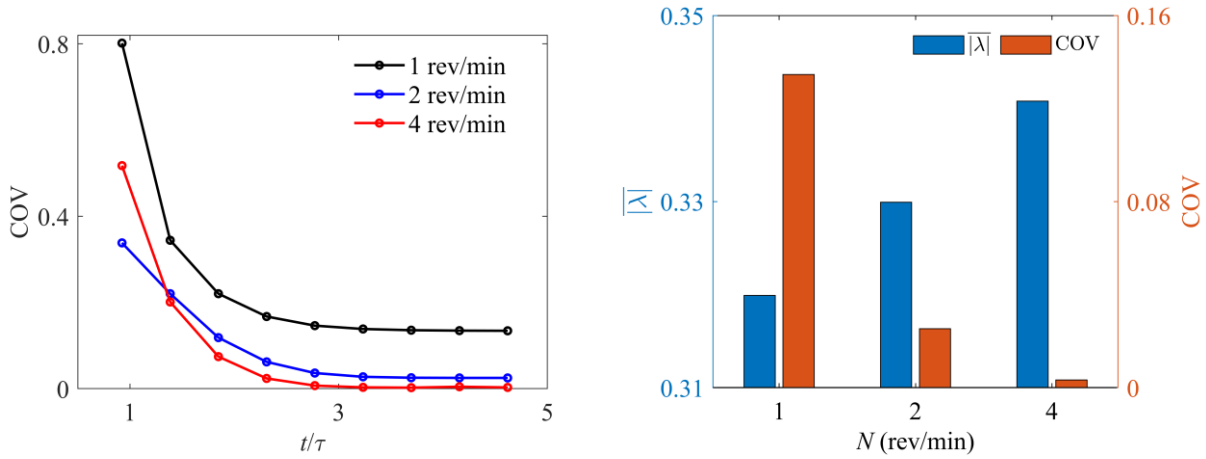

Fig. 15. Left panel: instantaneous COV of fluid 2 in the outlet plane at three rotor rotating speeds N. Right panel: the volume averaged $|\lambda|$ and COV of fluid 2 in the outlet plane at three rotor rotating speed with t/τ=4.5. The operation condition for the two panels is Q=640 mL/min, μ=20 Pa·s.

5.3.3 Effect of fluid viscosity on mixing performance

The left panel of Fig. 16 demonstrates the influence of fluid viscosity on the mixing performance. The COV values of cases with different fluid viscosity show slight differences in the early stages of the mixing process. As time progresses, the COV values become very close, confirming that the mixing of highly viscous fluid in this system is not dependent on viscosity. This finding is consistent with our previous observation in a lid-driven cavity[23].

Furthermore, the right panel of Fig. 16 compares the flow patterns of cases with different fluid viscosity with respect to the mixing performance. Interestingly, the volume averaged $|\lambda|$ is almost unaffected by the fluid viscosity, indicating that the flow pattern of highly viscous fluid in the dynamic mixer is not sensitive to changes in viscosity. Based on these findings, we can infer that the similarity in mixing performance is due to the similar flow motion of the fluids.

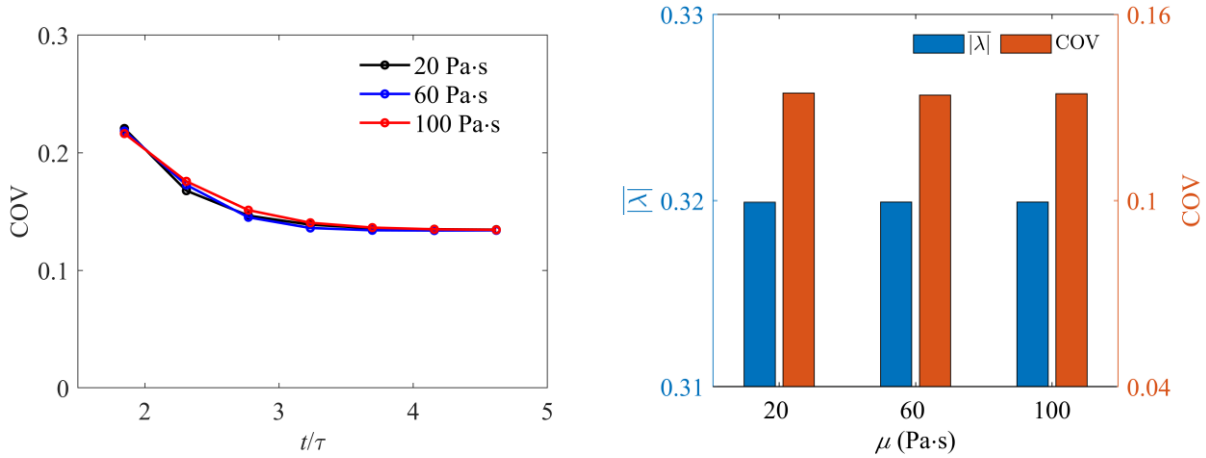

Fig. 16. Left panel: instantaneous COV of fluid 2 in the outlet plane at three fluid viscosity μ. Right panel: the volume averaged $|\lambda|$ and COV of fluid 2 in the outlet plane at three fluid viscosity with t/τ=4.5. The operation condition for the two panels is Q=640 mL/min, N=1 rev/min.

6 Conclusions

Flow patterns and mixing performance in a dynamic mixer were assessed through a combination of PLIF experiments and CFD simulations. To obtain the concentration field of the dynamic mixer, a refractive index matched technique was used in the experiment, which has not been reported before for a system like this. The experimental system has been carefully calibrated, and the measured concentration field could provide a valuable set of data for validating numerical models and methods.

In general, the simulated results align well with the experimental data, and any discrepancies between them were thoroughly discussed. The simulated flow patterns illustrate that the fluids experience extension, shearing, and stacking processes, promoting transfer phenomena in the dynamic mixer. The mixing index λ was used for evaluating the proportion of elongational flow and shear flow. Due to the spatially symmetric

geometry of the dynamic mixer, the flow field and λ distribution showed axial and circumferential periodicity.

Then, the experimentally validated simulation method was applied in investigating the mixing process under different conditions in terms of the coefficient of variation (COV) as a function of time. For highly viscous fluids, the mixing performance became better with lower feeding flow rate and higher rotating speed. It is interesting that the viscosity itself plays a marginal role in the mixing of highly viscous fluids. Not very surprising though, once the Reynolds number is well below 1 the flow becomes Re independent and since Sc is very large, numerical diffusion will not differ much between cases with different viscosity. The relationship between the flow pattern and the mixing characteristic was also considered quantitatively. After the mixing performance state achieves time-independence, the simulations consistently showed that an improvement of mixing (i.e. a reduction of COV) is associated with a slight increase of the volume averaged $|\lambda|$. This suggests that elongational flow is more effective than the shear flow in promoting the mixing of highly viscous fluid. These results could guide dynamic mixer design and assist optimization in developing high performance polymer.

Acknowledgements

The authors gratefully acknowledge financial support from the National Natural Science Foundation of China (No.22178014), and it was essential to the success of this research project.

Reference

(1) Todd, D. B. Mixing of Highly Viscous Fluids, Polymers, and Pastes. In *Handbook of Industrial Mixing*; John Wiley & Sons, Ltd, 2003; pp 987–1025. https://doi.org/10.1002/0471451452.ch16.

(2) Ottino, J. M.; Chella, R. Laminar Mixing of Polymeric Liquids; a Brief Review and Recent Theoretical Developments. *Polymer Engineering & Science* **1983**, *23* (7), 357–379. https://doi.org/10.1002/pen.760230702.

(3) Alvarez, M. M.; Zalc, J. M.; Shinbrot, T.; Arratia, P. E.; Muzzio, F. J. Mechanisms of Mixing and Creation of Structure in Laminar Stirred Tanks. *AIChE Journal* **2002**, *48* (10), 2135–2148. https://doi.org/10.1002/aic.690481005.

(4) Kolomiets, A.; Jirout, T. Analysis of the Dispersion of Viscoelastic Clusters in the Industrial Rotor-Stator Equipment. *Processes* **2021**, *9* (12), 2232. https://doi.org/10.3390/pr9122232.

(5) Hindmarch, R. S. The Cavity Transfer Mixer: A Blender for All Seasonings. *Materials & Design* **1987**, *8* (6), 331–339. https://doi.org/10.1016/0261-3069(87)90083-5.

(6) Wang, C.; Manas-Zloczower, I. Flow Field Analysis of a Cavity Transfer Mixer. *Polymer Engineering & Science* **1994**, *34* (15), 1224–1230. https://doi.org/10.1002/pen.760341509.

(7) Grosso, G.; Hulsen, M. A.; Sarhangi Fard, A.; Overend, A.; Anderson, P. D. Mixing Processes in the Cavity Transfer Mixer: A Thorough Study. *AIChE Journal* **2018**, *64* (3), 1034–1048. https://doi.org/10.1002/aic.15986.

(8) Huang, F.; Chen, P.; Wang, J.; Li, Z.; Gao, Z.; Derksen, J. J. Refractive Index-Matched PIV Experiments and CFD Simulations of Mixing in a Complex Dynamic Geometry. *Ind. Eng. Chem. Res.* **2020**, *59* (16), 7982–7992. https://doi.org/10.1021/acs.iecr.0c00169.

(9) Jaffer, S. A.; Bravo, V. L.; Wood, P. E.; Hrymak, A. N.; Wright, J. D. Experimental Validation of Numerical Simulations of the Kneading Disc Section in a Twin Screw Extruder. *Polymer Engineering & Science* **2000**, *40* (4), 892–901. https://doi.org/10.1002/pen.11217.
(10) Cortada-Garcia, M.; Weheliye, W. H.; Dore, V.; Mazzei, L.; Angeli, P. Computational Fluid Dynamic Studies of Mixers for Highly Viscous Shear Thinning Fluids and PIV Validation. *Chemical Engineering Science* **2018**, *179*, 133–149. https://doi.org/10.1016/j.ces.2018.01.010.
(11) Alberini, F.; Simmons, M. J. H.; Ingram, A.; Stitt, E. H. Use of an Areal Distribution of Mixing Intensity to Describe Blending of Non-Newtonian Fluids in a Kenics KM Static Mixer Using PLIF. *AIChE Journal* **2014**, *60* (1), 332–342. https://doi.org/10.1002/aic.14237.
(12) Ikarashi, Y.; Fujisawa, N. Mass Transfer Measurements and Flow Separation Behavior in a 90° Short Elbow. *International Journal of Heat and Mass Transfer* **2019**, *136*, 1106–1114. https://doi.org/10.1016/j.ijheatmasstransfer.2019.03.076.
(13) Yuki, K.; Hasegawa, S.; Sato, T.; Hashizume, H.; Aizawa, K.; Yamano, H. Matched Refractive-Index PIV Visualization of Complex Flow Structure in a Three-Dimentionally Connected Dual Elbow. *Nuclear Engineering and Design* **2011**, *241* (11), 4544–4550. https://doi.org/10.1016/j.nucengdes.2010.12.026.
(14) Zhu, L.; Cai, T.; Huang, J.; Stringfellow, T. C.; Wall, M.; Yu, L. Water Self-Diffusion in Glassy and Liquid Maltose Measured by Raman Microscopy and NMR. *J. Phys. Chem. B* **2011**, *115* (19), 5849–5855. https://doi.org/10.1021/jp202663r.
(15) Arbeloa, I. L.; Rohatgi-Mukherjee, K. K. Solvent Effect on Photophysics of the Molecular Forms of Rhodamine B. Solvation Models and Spectroscopic Parameters. *Chemical Physics Letters* **1986**, *128* (5), 474–479. https://doi.org/10.1016/0009-2614(86)80656-X.
(16) Crimaldi, J. P. Planar Laser Induced Fluorescence in Aqueous Flows. *Experiments in Fluids* **2008**, *44* (6), 851–863. https://doi.org/10.1007/s00348-008-0496-2.
(17) Irani, R. R.; Adamson, A. W. Transport Processes in Binary Liquid Systems. *J. Phys. Chem.* **1958**, *62* (12), 1517–1521. https://doi.org/10.1021/j150570a012.
(18) Hadžić, I.; Hennig, J.; Perić, M.; Xing-Kaeding, Y. Computation of Flow-Induced Motion of Floating Bodies. *Applied Mathematical Modelling* **2005**, *29* (12), 1196–1210. https://doi.org/10.1016/j.apm.2005.02.014.
(19) Hamidipour, M.; Chen, J.; Larachi, F. CFD Study and Experimental Validation of Trickle Bed Hydrodynamics under Gas, Liquid and Gas/Liquid Alternating Cyclic Operations. *Chemical Engineering Science* **2013**, *89*, 158–170. https://doi.org/10.1016/j.ces.2012.11.041.
(20) Ferziger, J. H.; Perić, M.; Street, R. L. Finite Volume Methods. In *Computational Methods for Fluid Dynamics*; Springer: Switzerland, 2020; pp 81–110. https://doi.org/10.1007/978-3-319-99693-6_4.
(21) Nakayama, Y.; Kajiwara, T.; Masaki, T. Strain Mode of General Flow: Characterization and Implications for Flow Pattern Structures. *AIChE Journal* **2016**, *62* (7), 2563–2569. https://doi.org/10.1002/aic.15228.
(22) Mandal, M. M.; Aggarwal, P.; Nigam, K. D. P. Liquid–Liquid Mixing in Coiled Flow Inverter. *Ind. Eng. Chem. Res.* **2011**, *50* (23), 13230–13235. https://doi.org/10.1021/ie2002473.
(23) Wang, J.; Ma, S.; Chen, P.; Li, Z.; Gao, Z.; Derksen, J. J. Mixing of Miscible Shear-Thinning Fluids in a Lid-Driven Cavity. *Chinese Journal of Chemical Engineering* **2022**, 58, 112–123. https://doi.org/10.1016/j.cjche.2022.10.004.

Contents graphic：